

Hourly impact of urban features on the spatial distribution of land surface temperature: A study across 30 cities



Qi Wang ^{a,*}, Haitao Wang ^b, Lanhong Ren ^c, Jianli Chen ^d, Xiaona Wang ^a

^a College of Landscape Architecture and Tourism, Hebei Agricultural University, Baoding, 071000, China

^b School of Architecture, Tianjin Chengjian University, Tianjin, 300384, China

^c College of Art & Design, Nanjing Tech University, Nanjing, 211816, China

^d Department of Civil and Environmental Engineering, University of Utah, Salt Lake City, UT 84112, USA

ARTICLE INFO

Keywords:

Diurnal cycle
Land surface temperature
Machine learning
Urban morphology
Google earth engine

ABSTRACT

Global warming and the urban heat island effect exacerbate excessive heat in urban environments, adversely impacting human health. Effective urban planning can mitigate these effects by influencing land surface temperature (LST). While previous studies have examined the influence of urban features on LST across seasons and between day and night, detailed hour-by-hour comparisons remain unexplored. This study addresses this gap by analyzing the hourly impacts of various urban features on LST in 30 U.S. cities using geostationary weather satellite data. We employed cloud-based analytics and machine learning techniques to aggregate data from thousands of images, identifying the relative importance and correlation curve of each urban feature on LST at each hour. Our findings revealed two distinct correlation patterns: dynamic daytime patterns with significant hourly variability and stable nocturnal patterns with minimal hourly differences. These results demonstrate that sunlight intensity greatly affects the correlation between urban features and LST. Urban planners should therefore consider broader patterns rather than focusing on specific hours. These insights provide valuable guidance for landscape and urban planners in developing strategies for climate adaptation and heatwave mitigation, contributing to the growing body of literature on sustainable cities.

1. Introduction

Urban environments, marked by their extensive replacement of natural landscapes with impermeable structures, exhibit significant differences from their rural counterparts in albedo, heat capacity, and evapotranspiration rates (Massaro et al., 2023). These changes result in the pronounced urban heat island (UHI) effect, characterized by temperatures that are markedly higher than those in surrounding rural areas (Oke, Mills, Christen & Voogt, 2017). The UHI phenomenon, intensified by global warming and urban expansion, exposes an ever-growing number of people to potentially life-threatening heat condition (Ullah et al., 2023; Yu et al., 2024). The implications of increased urban temperatures are far-reaching, affecting health, energy demand, carbon emission and economic productivity (Burke, Hsiang & Miguel, 2015; Gasparrini et al., 2017; Ramakrishnan, Wang, Sanjayan & Wilson, 2017;

Wei, He, Liu & Li, 2024; M. Zhang et al., 2023). Variations in urban temperatures, shaped by the thermal properties of materials, urban design, and human activities, create distinct thermal zones within cities, underscoring the complex interplay between urban features and thermal dynamics (Wu, Yu, Ma & Zhao, 2022). Grasping this complexity is crucial for devising strategies to counteract extreme heat, enhance urban climates, and ensure the health and economic wellbeing of urban populations in an era of escalating urbanization and climate change (Zhang, Shukui, Zhang & Chen, 2024).

Urban thermal environmental data are primarily derived from two sources: ground-based atmospheric temperature measurements from meteorological stations (Ho et al., 2014; Yan et al., 2014) and land surface temperature (LST) observations from remote sensing technologies (Lin, Xu, Yao, Yang & Yang, 2023; Ren et al., 2023). While air temperature data offer high temporal resolution and direct relevance to

Abbreviations: ALE, Accumulated Local Effects; ECOSTRESS, ECOsystem Spaceborne Thermal Radiometer Experiment on Space Station; EST, Eastern Standard Time Zone; GBM, Gradient Boosting Machine; GOES-16, Geostationary Operational Environmental Satellite-16; LST, Land Surface Temperature; MTH, Mean Tree Height; NLCD, National Land Cover Database; UHI, Urban Heat Island.

* Corresponding author at: Hebei Agricultural University, No. 2596, Lekai South Street, Lianchi District, Baoding, 071000, China.

E-mail address: wikiwang0421@hebau.edu.cn (Q. Wang).

<https://doi.org/10.1016/j.scs.2024.105701>

Received 10 April 2024; Received in revised form 12 July 2024; Accepted 23 July 2024

Available online 26 July 2024

2210-6707/© 2024 Elsevier Ltd. All rights are reserved, including those for text and data mining, AI training, and similar technologies.

human thermal comfort, their utility is limited by the considerable distances between weather stations, resulting in data sparsity (Chang et al., 2021; Lin, Xu, Yao, Yang & Ye, 2024). Conversely, remote sensing based LST are now favored for their ability to provide comprehensive regional to global coverage, high spatial resolution, and cost-effectiveness, making them more suitable for urban climate studies (Botje, Dewan & Chakraborty, 2022; Peng, Jia, Liu, Li & Wu, 2018; Song et al., 2020; Zhang, Tan, Liang, Zhang & Chen, 2024). Among the most widely used sensors for LST measurement are those aboard polar-orbiting satellites, including Landsat TM/TIRS, the Moderate Resolution Imaging Spectroradiometer (MODIS), and the Advanced Spaceborne Thermal Emission and Reflection Radiometer (ASTER) (Chang et al., 2021).

The spatial distribution of LST is shaped by a range of urban features. These factors mainly include: (1) landscape compositions, such as the proportions of vegetation, water, impervious surfaces, and other land-cover types (Lin et al., 2023; Zhang et al., 2023; Zhou et al., 2014); (2) surface biophysical parameters, notably the normalized difference vegetation index (NDVI) (Adeyeri et al., 2024; Guha, Govil, Dey & Gill, 2018; Logan, Zaitchik, Guikema & Nisbet, 2020); (3) Urban landscape patterns, including patch density (PD), edge density (ED) and landscape shape index (LSI) etc. (Cai, Yang, Zhang, Xiao & Xia, 2023; Peng et al., 2018; Zhou, Huang & Cadenasso, 2011); (4) three-dimensional urban structures, such as mean tree height, mean building height and sky view factor (SVF) (Alexander, 2021; Chen et al., 2023; Wang, Wang, Meng, Zhou & Wang, 2023); (5) Surface reflectivity, such as surface albedo (Dewan et al., 2021; Smith, Fabian & Hutyra, 2023); and (6) Socioeconomic factors, including population density, nighttime light intensity (NTL), and points of interest (POIs) (Bera, Chatterjee, Ghosh, Dinda & Bera, 2022; Song et al., 2020; Zhang, Yang, Ma, Xiao & Xia, 2023). These diverse urban elements are intricately linked to LST variations, highlighting the complex dynamics at play in urban thermal environments.

Traditionally, studies exploring the relationship between urban features and LST have employed regression analysis, including simple linear, multiple linear, and geographically weighted regression (Estoque, Murayama & Myint, 2017; Kashki, Karami, Zandi & Roki, 2021; Peng et al., 2018). However, given the inherent limitations of linear assumptions in these models, recent research has increasingly applied machine learning techniques such as random forest (RF), boosted regression trees (BRT), and extreme gradient boosting (XGBoost). (Lemus-Canovas, Martin-Vide, Moreno-Garcia & Lopez-Bustins, 2020; Logan et al., 2020; Lu, Fu, Dewan & Li, 2023; Pande et al., 2024). These non-parametric models, free from predetermined assumptions, excel at identifying nonlinear patterns between urban features and LST, while also evaluating the relative importance of various urban features.

Previous methodologies for LST analysis have predominantly utilized data from polar-orbiting satellites, such as Landsat, MODIS, and ASTER. These satellites, while invaluable for global environmental monitoring, are constrained by their temporal resolution, offering a maximum of one to two observations per day. Consequently, the dynamic interplay between urban features and LST has been largely explored through broad temporal lenses—seasonal shifts or day-versus-night comparisons. This approach, however, overlooks the nuanced fluctuations within the diurnal cycle, where sunlight intensity and urban landscape interactions significantly alter thermal patterns, potentially omitting critical insights into urban heat dynamics. In an innovative shift, a few studies have ventured into leverage data from the ECOSTRESS, mounted on the International Space Station (ISS). The unique, non-sun-synchronous orbit of the ISS allows ECOSTRESS to capture LST data across various times of day, offering a more granular view of thermal dynamics throughout the diurnal cycle. This approach has enabled researchers, including Han et al. (2023), Wang et al. (2023), and Lin et al. (2024) to expand the temporal resolution of LST observations to up to eight distinct time points within a single day. However, despite these advances, the data collection is constrained to discrete

moments—such as those specified in the study of Han et al. (2023) at 10:42, 14:13, 22:32, and 03:09—limiting a continuous analysis of the diurnal cycle. Moreover, the ISS's orbit introduces another layer of complexity, as ECOSTRESS captures images on different dates, potentially confounding the analysis with date-specific variability and not truly reflecting a continuous diurnal cycle. This limitation underscores a persistent challenge: accurately delineating how urban features impact LST distribution on an hourly basis throughout the day.

To bridge this research gap, our study capitalizes on the capabilities of the Geostationary Operational Environmental Satellite (GOES) series, notably the GOES-16 satellite, which was launched in late 2016 and has been operational since 2017. This initiative marks a substantial progression in obtaining continuous, high-quality, hourly Land Surface Temperature (LST) data across a spatial resolution of 2 km. In contrast to the limitations associated with earlier or concurrent satellite missions, which often suffer from limited temporal resolution—including instruments like ECOSTRESS—the GOES series delivers a consistent and frequent observational sequence (NOAA, 2019). Utilizing data from GOES-16 in conjunction with cutting-edge machine learning algorithms, this research pioneers the exploration of the dynamic interplay between urban landscapes and thermal conditions across diurnal cycles. This study is, to our knowledge, the first to analyze the hourly correlations between urban features and the spatial variation of LST, offering new insights into the complexities of urban heat dynamics.

Besides improving diurnal resolution to 24 h, we also enhanced previous studies on the methodologies. We extend the geographic scope of our study beyond the one or few cities typical of earlier machine learning-based studies (Lemus-Canovas et al., 2020; Lin et al., 2024; Logan et al., 2020), incorporating data from 30 cities to enable a comprehensive analysis that yields broadly applicable insights rather than outcomes limited to specific urban settings (Tang, Liu, Tian, Zhao & Dai, 2023). To address the challenges posed by daily observations variations, we employ advanced cloud-based processing to amalgamate thousands of images—such as those used for calculating surface albedo from Landsat—to produce a composite image. This strategy, diverging from the single-image approaches prevalent in prior research (e.g. Chen, Wang, Bao, Luo & Wei, 2022; Lin et al., 2023; Wang, Wang, Zhou, Liu & Wang, 2022), ensures consistency in representing average conditions, thereby mitigating the variability and uncertainty characteristic of individual snapshots. Furthermore, our statistical modeling approach introduces a significant methodological refinement over existing practices, which often rely on fixed hyperparameters or simple random sampling (Chen et al., 2022; Li & Hu, 2022; Zeng et al., 2022). By implementing cross-validation to fine-tune hyperparameters and employing stratified sampling to ensure data representativeness, alongside the use of accumulated local effects (ALE) for a nuanced examination of the impact of urban features on LST (Molnar, 2020), we effectively reduce the influence of correlated variables, and enhancing the precision and reliability of our analysis.

With these enhancements, we seek to answer the question: “*What is the influence and relative importance of urban features on the spatial variation of land surface temperature, and how does this correlation change hour by hour?*” To achieve this, we selected 30 cities within the Eastern Standard Time Zone (EST) of the U.S. and employed nonlinear statistical methods to explore the impact of urban features on 24-hour LST during the summer months. Specifically, the main objectives of the study were: (1) To compare the spatial pattern of LST at different hours of the diurnal cycle. (2) To assess how LST changes across different types of land cover hourly. (3) To evaluate the relative importance of various urban features to the spatial distribution of LST in the 24-hour cycle. (4) To analyze the non-linear impact patterns of the most important urban features on LST throughout the day. By undertaking this nuanced analysis, we do not presume to establish causality but rather to enhance the granularity of our understanding of urban thermal dynamics. The insights gleaned promise not only to deepen our knowledge of the mechanisms driving urban heating but also to inform strategies aimed at reducing the impact

of heatwaves. Consequently, this research bears implications for urban planning and climate adaptation efforts, positioning cities to better withstand and respond to rising temperatures in an era of climate change.

2. Study area and data collection

2.1. Study area

In this study, we selected 30 cities situated in the eastern United States (U.S.). Given the continental expanse of the U.S., which encompasses four distinct time zones, our analytical framework necessitated a uniform temporal schema, anchored to the Eastern Standard Time (EST), to accurately monitor diurnal thermal variances attributable to solar radiation. This selection criterion was pivotal for elucidating the diurnal cycle in a coherent manner. The geographical span of these cities is extensive, ranging between longitudes 70°W to 86°W and latitudes 25°N to 44°N (Fig. 1), thereby offering a comprehensive scope for sampling and facilitating a robust analysis. The selection notably includes metropolitan areas most susceptible to the urban heat island effect, such as New York, Philadelphia, Charlotte, Miami, among others. The climatic diversity within this domain is represented by 3 principal climatic zones: Cfa (Humid subtropical climate), Dfa (Hot-summer humid continental climate), and Dfb (Warm-summer humid continental climate). This diverse climatic assemblage, coupled with a broad latitudinal and geoclimatic spectrum, ensures the applicability of our findings across a wide range of environmental conditions. To concentrate our analysis on urban parameters, a circular area with a diameter

of 70 km was delineated for each city, encompassing a cumulative surface area of $115,817 \text{ km}^2$ and a populace of 56 million.

2.2. Hourly land surface temperature data

Our study aimed to unravel the intricate relationship between urban features and the diurnal patterns of LST throughout the summer period, leveraging regression analysis to scrutinize variations across each hour of the day. Within this analytical paradigm, LST was designated as the dependent variable, with various urban features serving as the independent factors. The core LST dataset was procured from the GOES-16 Advanced Baseline Imager (ABI) Level 2 Land Surface Temperature product for the Continental United States (CONUS), notable for its 2 km spatial and hourly temporal resolutions. This dataset, generated through the employment of the ABI spectral bands 14 ($11.2 \mu\text{m}$) and 15 ($12.3 \mu\text{m}$) via the split-window technique, is distinguished by its rigorous validation against both in situ observations and cross-referencing with data from other sensors like VIIRS-SNPP, MODIS-AQUA, and MODIS-TERRA (Chang et al., 2021).

The data retrieval was conducted through Amazon Web Services (AWS) (Table 1), employing a Python script. To craft a continuous, cloud-free, and comprehensive depiction of summer LST distribution, we selected imagery from June 1 to August 31, 2022—conforming to the meteorological definition of summer—and calculated the average LST values for each hour over this three-month span. Areas covered by clouds were assigned a 'no data' status and consequently omitted from the analysis, ensuring that our averages were derived solely from valid data points. This methodology facilitated the replacement of cloud-

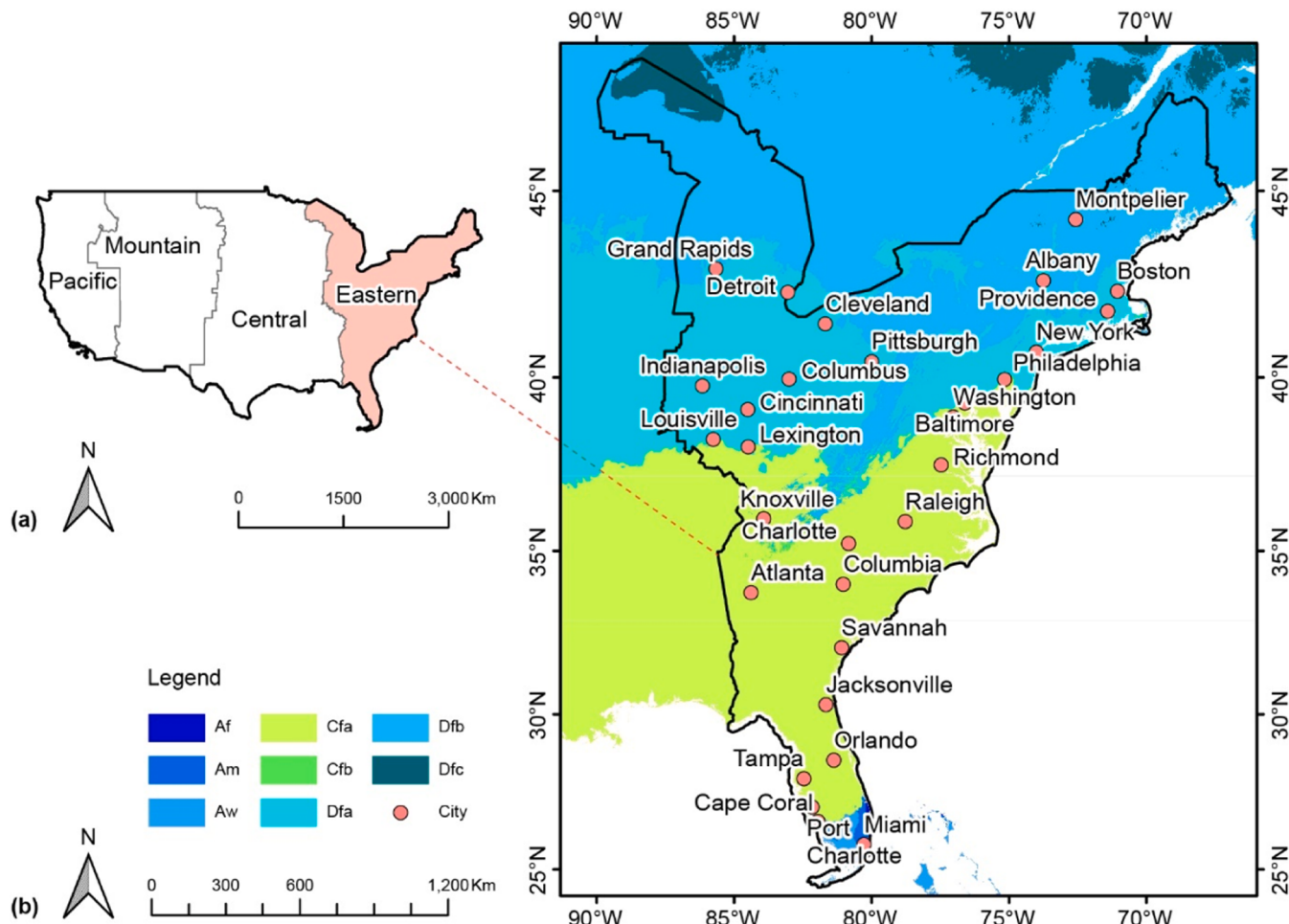


Fig. 1. Study area. (a) Location of Eastern standard time zone; (b) Cities studied and climate zone distribution in the study area.

Table 1

Data used in this study.

Categories	Data	Spatial resolution	Date	Usage	URL
Remote sensing images	GOES-16	2km	2022-06-01 to 2022-08-31	Hourly LST	https://noaa-goes16.s3.amazonaws.com/index.html
	Landsat 8	30m	2021-06-01 to 2021-08-31 2022-06-01 to 2022-08-31 2023-06-01 to 2023-08-31	Surface albedo calculation	GEE Image Collection ID: "LANDSAT/LC08/C02/T1_TOA"
Geographical information data	Microsoft building open dataset	Polygon vector	2023-05-18	Percentage of the building footprints calculation	https://github.com/microsoft/GlobalBuildingFootprints
	NLCD	30m	2021	Landscape compositions and landscape patterns calculation	https://www.mrlc.gov/
	GFCH	30m	2019	Mean tree height calculation	https://glad.umd.edu/dataset/gedi
	Worldpop	100m	2020	Population density calculation	https://www.worldpop.org
	SRTM	1 arc-second	2000	Average elevation calculation	GEE Image Collection ID: "USGS/SRTMGL1_003"
	Köppen-Geiger Global 1-km climate classification maps	30 arc-second	2018	Köppen-Geiger Climate zone identification	https://www.globo2.org/koppen/

obscured areas with valid data, yielding seamless, cloud-free images. Following the processing of over 2000 images, we synthesized 24 distinct images, each representing the average LST value for a particular hour, as illustrated in Fig. 2.

2.3. Urban features data

2.3.1. Land cover

Land cover data for our analysis were sourced from the National Land Cover Database (NLCD) for the conterminous U.S., 2021 edition. Developed collaboratively by the U.S. Geological Survey (USGS) and the Multi-Resolution Land Characteristics (MRLC) Consortium, the NLCD offers comprehensive, nationwide coverage of land cover at a spatial resolution of 30 m. This dataset employs a modified Anderson Level II classification system, presenting a categorization of 8 primary classes and 20 subclasses (Dewitz, 2023). The download URL is <https://www.mrlc.gov/>. An illustrative excerpt of this dataset, focusing on Cleveland, is depicted in Fig. 4(a). Utilizing this detailed land cover information, various classification schemes were used to analyze the landscape composition and configurations, as elaborated in Section 3.2.

2.3.2. Building footprints

Building footprints utilized in our study were sourced from the open-access Microsoft Building Dataset. This dataset was delineated from Bing Maps through the application of deep neural networks. It has been demonstrated that this dataset achieves a precision of 88.3% in North America when compared to the Geo-Wiki built-up surface validation dataset (Herfort, Lautenbach, Porto De Albuquerque, Anderson & Zipf, 2023). We download These polygons from the Global ML Building Footprints GitHub repository (<https://github.com/microsoft/GlobalMLBuildingFootprints>) via a Python script. It is continuously updated. For our research, we used the version updated on May 18, 2023. Owing to the expansive nature of our study area, the count of building footprint polygons exceeded 20,000,000. To manage this large dataset, Google Earth Engine (GEE) were leveraged for cloud-based statistical computations, effectively reducing what could have been days of computationally intensive work on personal computers to mere seconds. Fig. 3(a) presents a sample of the building footprints used in our analysis.

2.3.3. Landsat 8

We utilized the USGS Landsat 8 Level 1, Collection 2, Tier 1 dataset for surface albedo calculation. This dataset is accessible through the Google Earth Engine (GEE) Image Collection (ID: "LANDSAT/LC08/C02/T1_TOA"), and has a spatial resolution of 30 m. To mitigate potential biases from using singular imagery, we integrated as many

Landsat images as possible to reduce this uncertainty. This approach was facilitated by the efficiency of cloud-based computations of GEE, enabling the rapid processing and cloud removal from thousands of images through simple coding. We averaged Landsat images from June 1st to August 31st, across the years 2021 to 2023 (aligning with the temporal scope of our GOES-16 LST data). Cloud and shadow areas were excluded based on the 'QA_PIXEL' band of each image, ensuring the aggregation of only valid data. This method effectively minimized the impact of outliers and cloud contamination. After averaging 2109 images, the resultant dataset was seamless, unbiased, and free from cloud interference.

2.3.4. Forest canopy height and population data

Global Forest Canopy Height (GFCH) dataset (2019) was used to derive tree height, as depicted in Fig. 3(b). Constructed through the synthesis of Global Ecosystem Dynamics Investigation (GEDI) lidar data on forest structure and the time-series of Landsat analysis-ready data, this dataset provides a global forest canopy height map at a spatial resolution of 30 m. Its accuracy was validated against GEDI validation dataset (RMSE = 6.6 m; MAE = 4.45 m, R2 = 0.62), attesting to its high level of precision (Potapov et al., 2021). The download URL is <https://glad.umd.edu/dataset/gedi>.

Population distribution data were sourced from WorldPop, which provides open access to high-resolution (100 m) spatial demographic datasets (<https://www.worldpop.org/>). This dataset was constructed using a Random Forest-based dasymetric redistribution approach, integrating multiple datasets (Stevens, Gaughan, Linard & Tatem, 2015). Our study employed the WorldPop global project 2020 dataset, which was downloaded from Google Earth Engine (GEE) using the Image ID "WorldPop/GP/100 m/pop".

2.3.5. Geoclimatic dataset

Topographic elevation data were obtained from the Shuttle Radar Topography Mission (SRTM), providing digital elevation models with a resolution of 1 arc-second. This equates to approximately 28 m in urban areas like Miami and narrows to about 22 m in locations such as Montpelier. The data is accessible through Google Earth Engine, under the Image ID: "USGS/SRTMGL1_003".

Climate categorization employs the Köppen-Geiger climate classification system, an established framework conceived by Wladimir Köppen and subsequently refined by Rudolf Geiger. This system, recognized globally for its detailed classification of climate zones, divides climates into five primary groups and thirty subtypes. These categories are meticulously defined by specific monthly temperature and precipitation thresholds, facilitating a comprehensive and nuanced understanding of

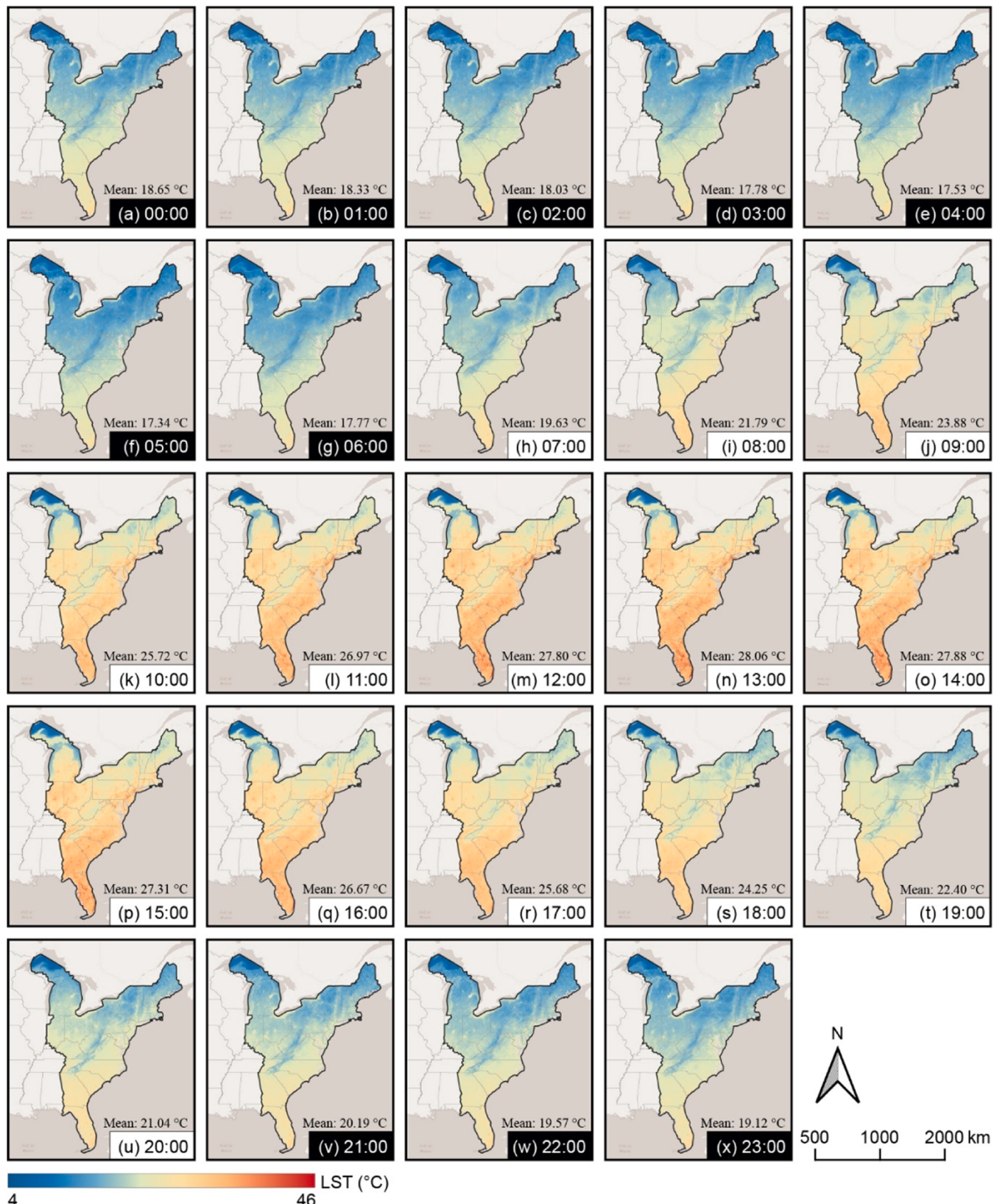


Fig. 2. 24-hour LST distribution in EST time zone of U.S. (a) – (x) represent the hourly LST distribution from 00:00 to 23:00 EST. Notably, for July 15th, 2022, sunrise and sunset times for Indianapolis span from 06:29 to 21:11, and for Boston from 05:20 to 20:19. Consequently, the period from 07:00 to 20:00, witnessing ubiquitous solar presence across the longitudinal extent, is designated as daytime (highlighted in white), whereas the interval from 21:00 to 06:00 is categorized as nighttime (highlighted in black).

global climate patterns (Beck et al., 2018) (Fig. 1b). We used the 2018 version from its official site (<https://www.globo20.org/koppen/>).

The datasets detailed above are comprehensively cataloged in Table 1 for reference. To ensure precise area calculations critical for the assessment of urban feature factors, all maps were standardized using the Albers conical equal area projection.

3. Methods

3.1. Analysis unit

To study the relationship between urban features and LST, we segmented the study area into basic analytical units. The utilization of GOES-R LST data, characterized by a larger cell size (approximately 4 km²) and a unique geostationary projection method, presented significant challenges in data summarization. However, this larger pixel size, surpassing that of other images, facilitated the aggregation of data from diverse sources without being influenced by their varying pixel sizes (all urban features were computed using average or proportion methods). Consequently, this dataset was designated as our foundational basis for the analytical units. It was converted into polygonal units using the "raster pixels to polygons" tool in QGIS. This conversion process ensured that the polygons perfectly aligned with the raster grid, providing a precise representation of LST (Fig. A1). Each analytical unit represented a unique observation for further regression analysis. All the data, including the average LST (the dependent variable) and various urban features (the independent variables), were calculated within each of the analytical units.

3.2. Urban features calculation

In this research, leveraging the urban features dataset delineated in Section 2.3, we embark on a quantitative exploration to elucidate urban features through the lens of urban feature factors. Our investigation encompasses four pivotal categories of factors: landscape composition, landscape patterns, geoclimatic conditions, and additional crucial factors including socioeconomic elements and 3D structural features. These domains are encapsulated by 17 potential factors influencing LST, selected based on criteria such as theoretical significance, broad applicability, ease of data acquisition, and minimal redundancy (Yao et al., 2022). An exhaustive delineation of the urban thermal environmental factors under scrutiny is presented in Table 2.

The assessment of landscape compositions and patterns was conducted using the R package "landscapemetrics." This comprehensive package serves as an effective alternative to the widely recognized FRAGSTATS software for landscape analysis (Hesselbarth, Sciaiani, With, Wiegand & Nowosad, 2019). Our analysis utilized the NLCD as the foundational land cover map, employing various combinations of land cover types to compute distinct metrics for each landscape attribute (Table 2). The calculation of landscape compositions, with the exception of P_building, was performed using the percentage of landscape of class (PLAND) metric. To characterize landscape patterns, we applied three distinct metrics: the Shannon's Diversity Index (SHDI), Patch Density (PD), and Shape Index (SI), which respectively measure landscape diversity, patch fragmentation, and shape complexity. The mathematical formulations for these metrics are provided below:

$$SHDI = - \sum_{i=1}^m (P_i * \ln P_i) \quad (1)$$

$$PD = N/A * 10000 * 100 \quad (2)$$

$$SI = \left(\sum_{j=1}^N (0.25 * P_j / \sqrt{a_j}) \right) / N \quad (3)$$

Where P is the proportion of land cover class i ; N is the number of

Table 2
Influencing factors selected in this study.

Categories	Name	Description	Range or unit
Landscape compositions ^a	Percentage of building footprints (P_Building)	Building footprint coverage (%) in a grid.	0–100%
	Percentage of tree area (P_Tree)	Tree canopy coverage (%) in a grid.	0–100%
	Percentage of non-tree vegetation area (P_NTveg)	Shrubs, grasses and herbs etc. coverage (%) in a grid.	0–100%
	Percentage of water area (P_Water)	Water area coverage (%) in a grid.	0–100%
	Shannon's diversity index (SHDI)	A measure of diversity for landscapes in a grid. This metric calculation used all the classes in NLCD.	—
	Patch density (PD)	Patch density of impervious surface, vegetation and water area in a grid, represented by PD_ISA, PD_Water, and PD_Veg respectively.	N/100 ha
Landscape patterns	Mean shape index (SI)	Mean shape index of impervious surface, vegetation and water area in a grid, represented by SI_ISA, SI_Water, and SI_Veg respectively.	—
	City	The city of the grid.	—
Geoclimatic conditions ^b	Climate zone (CZ)	Köppen-Geiger climate zone of the grid.	—
	Digital elevation model (DEM)	Average elevation of the grid.	M
	Mean tree height (MTH)	Average tree height in a grid.	m
Other factors	Surface albedo (Albedo)	The average surface reflectivity in a grid.	—
	Population (POP)	Population density within a grid.	people/ha

^a We amalgamated the landscape composition categories from the NLCD into trees, non-tree vegetation, water, and impervious surfaces. Upon integrating building footprints, our refined landscape composition parameters comprise the percentage of building footprints (P_Building), percentage of tree area (P_Tree), percentage of Non-Tree Vegetation area (P_NTveg), percentage of water area (P_Water), and the percentage of non-building impervious area (P_NBISA). However, utilizing a 100% allocation among the first four metrics enables the facile derivation of the latter, thus posing a risk of engendering multicollinearity in later analytical model. To obviate this issue, P_NBISA was excluded.

^b Geoclimatic conditions are designated as control variables; they will be incorporated within the model yet not considered in the analysis of urban feature performance. This strategy enables us to concentrate on examining the effects of other, non-geoclimatic factors on LST. To elucidate how various features affect predictions, we employ Accumulated Local Effects (ALE) plots. These plots are instrumental in visualizing the impact of individual features across their distribution, while simultaneously adjusting for the interplay of all other variables within the model. By leveraging this methodology, we are able to isolate and understand the specific contributions of urban features to LST under consistent geoclimatic conditions.

patches of the specific land cover class; A is the total landscape area (m²); P_j is the perimeter (m) of patch j and a_j is the area (m²) of patch j . The above calculations were performed in each of the analysis grids.

SHDI quantifies the diversity of land cover within a landscape. Its value starts at 0 for landscapes with a monoculture and increases with the introduction of additional land cover types. PD serves as a measure of landscape fragmentation, effectively describing how dispersed a land cover class is across a landscape. High values of PD suggest that patches of the land cover class in question are more scattered, indicating greater fragmentation. The SI reflects the average complexity of the shapes of land cover patches. A higher SI indicates that the edges of patches are relatively long in comparison to their area, suggesting more intricate or

convoluted shapes.

Geoclimatic conditions exert a significant influence on the distribution of LST, particularly in analyses spanning extensive areas. The oblate spheroidal shape of the Earth, coupled with its complex atmospheric dynamics, results in uneven thermal conditions across its surface. Given that these geoclimatic factors are immutable within the context of urban planning, they were designated as control variables in our investigation. Cities were used to define locations of the analysis grids. It condenses the information of longitude and latitude. Climate zone information was derived from Köppen-Geiger climate classification data. In cases where an analysis grid spanned multiple climate zones, the zone covering the largest portion of the grid was selected as its representative climate class. DEM data sourced from the SRTM, were averaged for each grid, providing an additional layer of contextual environmental information.

MTH and Population were derived by averaging data from GFCH and Worldpop data respectively. Surface albedo was calculated based on the seamless and cloud free averaged Landsat 8 data (Section 2.3.3). It used Landsat shortwave albedo calculation method developed by Liang (2001) and normalized by Smith (2010) (Fig. 3c).

3.3. Sample analysis

Our initial analysis focused on examining the overarching distribution of LST within the EST zone to understand the macro-level patterns of LST variation. Although this large-scale perspective on LST distribution provides insights into general trends, it does not elucidate the LST dynamics across different land cover types. To offer a more nuanced glimpse into these dynamics, we selected Cleveland as a focal point. Within this area, we pinpointed six locations that epitomize the primary land cover categories: developed areas with high, medium, and low urban intensity; deciduous forests; grasslands, comprising cultivated crops and hay/pasture areas; and water areas. Monitoring LST changes at these sites over a 24-hour cycle provided a concise yet informative view of our data, showing the thermal characteristics unique to each land cover type (Fig. 4).

3.4. Statistical models

As a non-linear machine learning model, Gradient boosting machine (GBM) was employed to construct regression models with LST as the dependent variable and 17 urban attributes as independent variables. As an ensemble technique, GBM excels at identifying nonlinear

relationships between dependent and independent variables (Friedman, 2001). Previous study has demonstrated that GBM outperformed models such as random forest (RF), artificial neural network (ANN), and multivariate adaptive regression splines (MARS), but its predictive accuracy was not far from that of the others (Wang et al., 2023). For this reason, we ultimately selected only the GBM model. Our analysis encompassed 24 GBM models, each predicated on the LST data of a single hour. In non-linear models such as GBM, a paucity of observations can precipitate overfitting, wherein the model demonstrates high performance on training data but fails to generalize effectively to unseen data (Molnar, 2020). Following the calculation of variables and the subsequent removal of null values, we secured a dataset comprising 27,374 observations. This substantial dataset size effectively mitigates the risk of overfitting, ensuring robust model performance across unseen data. Analysis revealed that the variance inflation factor (VIF) (O'Brien, 2007) scores of our data were under 10, indicating minimal multicollinearity. The data of each hour were partitioned into a 70% training set and a 30% testing set using stratified sampling (Trost, 1986), which safeguards against data leakage and ensures that the distribution of the testing dataset mirrors that of the training dataset. To further diminish overfitting risk and enhance model accuracy, we applied repeated 5-fold cross-validation for hyperparameter tuning (Fig. A2). This process relied on minimizing the root mean square error (RMSE) to ascertain the optimal hyperparameter combination for each hourly model (Refaeilzadeh, Tang & Liu, 2009). Geoclimatic factors were recognized for their significant influence on LST over large areas and were thus classified as control variables due to their static nature in urban planning contexts. Two sets of models for each hour LST were constructed for model performance comparison, one inclusive of all variables and the other excluding geoclimatic factors.

3.5. Model explanation

After constructing our models, we applied permutation-based importance techniques to determine the significance of urban features. In this approach, the values of each explanatory variable were randomly shuffled while keeping all other variables constant. Then the model performance was re-evaluated, typically by computing the increase in RMSE. A larger increase in RMSE indicates a higher importance of the variable in the model (Fisher, Rudin, & Dominici, 2019). The foremost impactful five factors for each hourly dataset were identified for further analysis regarding their influence on LST via Accumulated Local Effects

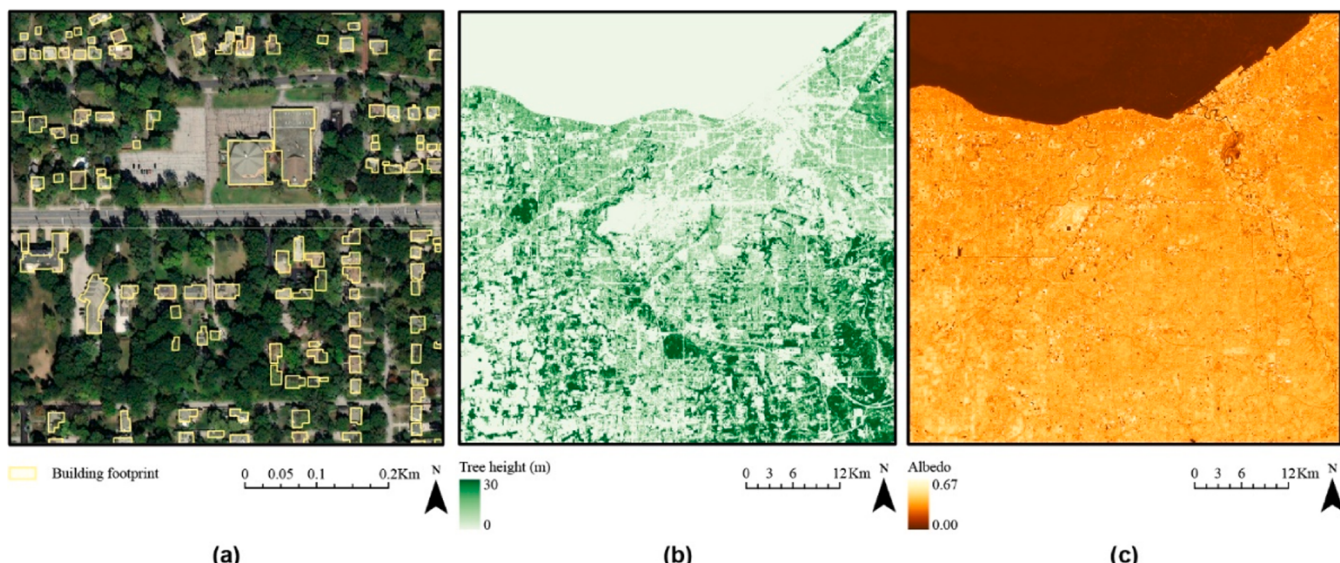


Fig. 3. Spatial distribution of urban features in part of Cleveland. (a) Building footprints; (b) Tree canopy height; (c) Surface albedo.

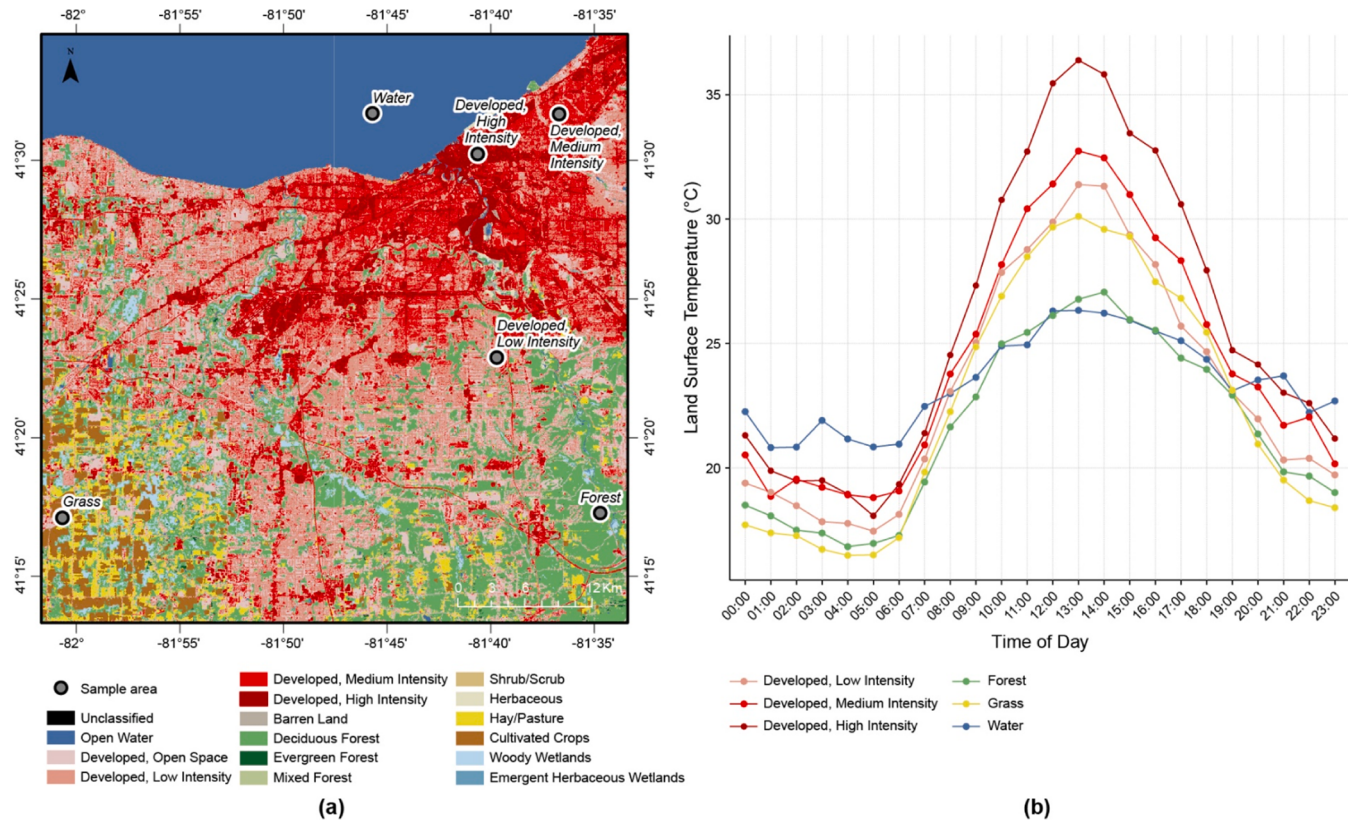


Fig. 4. 24-hour LST behavior on sampled area of Cleveland. (a) Land cover map and local sample points of Cleveland. (b) 24-hour LST cycle by land cover class in Cleveland. For consistency, the colors of land cover classes in (b) are the same as (a).

(ALE). ALE plots show effects of individual features on the prediction of a model across its domain, while accounting for the average effect of all other features (Molnar, 2020). This approach serves as a sophisticated counterpart to Partial Dependence Plots (PDPs), which are predicated on the assumption that explanatory features are non-correlated—a condition seldom met among urban features.

4. Results

4.1. Spatial distribution of 24-hour LSTs

Fig. 2 illustrates the diurnal distribution of LSTs across EST of the contiguous U.S. During nighttime hours (21:00 to 06:00), the LST remained relatively stable, fluctuating between 17.34 °C and 20.19 °C. This stability was disrupted at sunrise (circa 07:00), with LSTs rapidly escalating to peak at 28.06 °C by 13:00. A pronounced plateau above 25 °C was observed from 10:00 to 17:00, followed by a steep decline into the evening, underscoring the significant influence of solar radiation on LST dynamics. A pronounced latitudinal temperature gradient was observed, with northern areas consistently cooler than their southern counterparts, regardless of the time of day. This gradient was accentuated by diurnal solar movements, where the east warmed first at sunrise, though interestingly, it did not exhibit a commensurate cooling pattern at sunset, indicating a rapid heating but slow cooling phenomenon across the region. In contrast, water areas displayed negligible temperature fluctuations throughout the day. Specifically, the northeastern section of the EST zone, encompassing Lake Superior and Lake Michigan, maintained lower temperatures, underscoring the moderating effect of large water bodies on local climate variability.

Fig. 4(a) shows the land cover map and sample point locations, and Fig. 4(b) shows the LST behavior on each sample point in the 24-hour cycle. Across all locations, LST exhibited significant variability during

daylight hours, stabilizing through the night. Urban areas, stratified by development intensity, demonstrated a broad spectrum of temperature dynamics. Notably, LST in high intensity developed areas peaked at 36.39 °C at 13:00, marking a pronounced min-max temperature difference of 18.32 °C. Conversely, natural and semi-natural landscapes such as grasslands and forests registered more subdued temperature shifts, with grasslands and forests showing min-max temperature differences of 13.63 °C and 10.23 °C, respectively. Water bodies were characterized by the most uniform temperature profile throughout the day, ranging from a nocturnal low of 20.81 °C to a midday high of 26.33 °C, a variation of merely 5.52 °C. This underlines water's thermal inertia compared to terrestrial land covers, maintaining higher temperatures during nocturnal hours. Remarkably, areas within human settlements almost consistently recorded temperatures above 30 °C during maximum solar irradiance hours (12:00–14:00). The LST observations at 13:00 underscored a stark thermal contrast across different land covers, with high intensity developed areas exhibiting temperatures approximately 10.06 °C higher than water and forest areas. This highlights the pronounced effect of urban structures in amplifying local temperature conditions, particularly under the influence of peak solar energy.

4.2. Model performance

The comparative analysis of R^2 and RMSE values for two distinct model groups—those incorporating all variables and those excluding geoclimatic variables—on the unseen 30% test dataset is depicted in Fig. 5. The R^2 values, as illustrated in Fig. 5a, underscore the significant explanatory power of urban features, with R^2 values ranging from 0.92 to 0.98. This range indicates an exemplary fit between predicted and observed LST values, denoting high model accuracy. The RMSE values, spanning from 0.38 to 1.01, further affirm the model's precision, delineating an average prediction error slightly exceeding 1 °C at

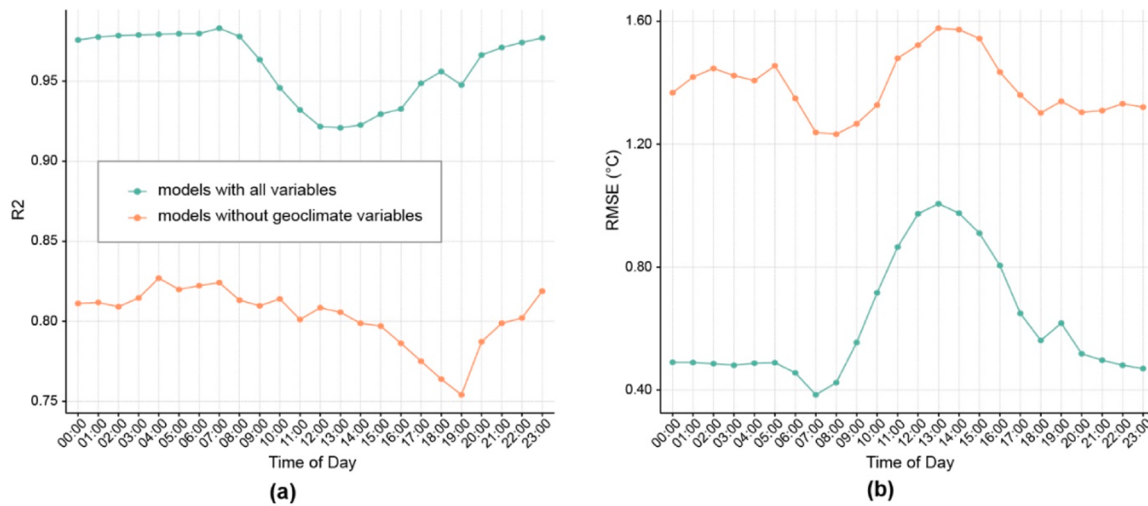


Fig. 5. Model performance comparison: models with all variables vs. models without geoclimate variables. (a) R² comparison. (b) RMSE comparison.

maximum deviation.

Exclusion of geoclimatic variables resulted in a notable decline in model performance, with R² values diminishing to a range of 0.75 to 0.83, and RMSE values escalating to between 1.23 and 1.58. This variance highlights the critical role of geoclimatic variables as control variables in enhancing model accuracy. Nonetheless, even in the absence of geoclimatic inputs, the models retained commendable predictive capacity. A discernible decrease in model efficacy was observed during the peak sunlight hours of 10:00 to 16:00 for both model groups, suggesting a more complex interaction between variables during these times.

4.3. Relative importance ranking

Fig. 6 displays the permutation-based importance of urban features on LSTs across a 24-hour cycle. Notably, surface albedo emerged as the principal factor during nighttime, consistently securing the highest rank from 21:00 to 06:00. Although decreased, its influence persisted into the daytime, remaining within the top five influencers across all hours. P_Building predominated during daylight, attaining the foremost rank in 11 out of the 14 daytime hours. Although its effect was moderated at night, its impact was still non-negligible, especially between 21:00 and 23:00, where it ranked third to fourth. Vegetative and aquatic landscapes, quantified by the percentage of areas covered by trees, grass, and water (P_Tree, P_NTveg, P_Water), exerted a notable impact on LST, ranking within the top five for most hourly intervals during both day and night. Notably, P_NTveg stood out as the second most influential factor throughout the night, while P_Tree frequently secured the second to third rank during daylight hours. Landscape configurations like PD, SI and SHDI had comparatively lower impact on LST, with an exception of SHDI ranked top five at the nighttime. The influence of mean tree height (MTH) on LST exhibited significant temporal variability. While its contribution to LST was not pronounced during the night, it experienced a marked increase in importance with the dawn, ascending to the second rank by 07:00, aligning with sunrise. This elevated significance began to diminish after 11:00; however, MTH remained a top-five influencing factor until the evening approached at 19:00. Population density (POP), in comparison, consistently demonstrated a moderate influence on LST across all daytime periods.

4.4. Correlation patterns

Fig. 7 delineates the correlation patterns between urban features and LST through ALE plots, offering insight into the marginal effects of urban features on LST across a 24-hour cycle. ALE values, plotted on the y-axis,

quantify the influence of specific urban feature variations on LST predictions, while controlling for other variables.

Our analysis identified landscape compositions, Albedo, Mean Tree Height (MTH), and Shannon's Diversity Index (SHDI) as pivotal determinants of LST variability within the diurnal cycle. Notably, P_Building emerged as a dominant factor during daylight hours, especially amid peak solar intensity (11:00–15:00). It was positively correlated with LST from 7:00 to 22:00, characterized by non-linear response curves. Specifically, the maximal effect of P_Building on LST was observed when its value was below 15%, after which the curves turned flatter. Conversely, P_Water demonstrated a consistent negative correlation with LST throughout the diurnal cycle, impacting LST in a predominantly linear fashion. The influence of P_NTveg was most significant during night hours, effectively reducing LST. The corresponding ALE plots revealed smooth, downward concave curves without marked inflection points, suggesting that minor proportions of P_NTveg exert disproportionately larger cooling effects on nocturnal LST. Tree coverage (P_Tree) exhibited a consistent negative correlation with LST across the entire diurnal cycle. This relationship was largely linear during daylight hours and transitioned to a downward concave pattern throughout the night. Albedo's correlation with LST was positively marked during daylight and inversely related at night. The correlation patterns of albedo were not linear, and the maximum effect of it was between 0 and around 0.13 (albedo of water), beyond which the impact plateaued across all hours. The role of Mean Tree Height (MTH) in modulating LST was subtle at night yet significantly pronounced during the day. Beginning with an ALE value of 0.5 °C at 7:00, the effect of MTH on LST escalated to 2 °C by 10:00, reaching a zenith of up to 2.5 °C at 15:00 before receding to 0.5 °C by 18:00. Shannon's Diversity Index (SHDI) exhibited no significant daytime influence on LST. However, its nocturnal effects were characterized by positive, upward concave trajectories.

4.5. 24-Hour trending of the impact of urban features on LST

The ALE plots are complex, and their time trends are not immediately apparent (Fig. 7). Therefore, Fig. 8 was created to illustrate the hourly trends of the maximum ALE differences for each urban feature. The impacts of various urban features varied at different hours, exhibiting distinct trend patterns. There were four main types of influence trends: (1) Always positive: Variables such as P_Building and SHDI consistently showed positive impacts on LST throughout the diurnal cycle. Notably, the impact of P_Building peaked at noon, influencing LST by up to 3 °C, which was the highest effect among all urban features. (2)

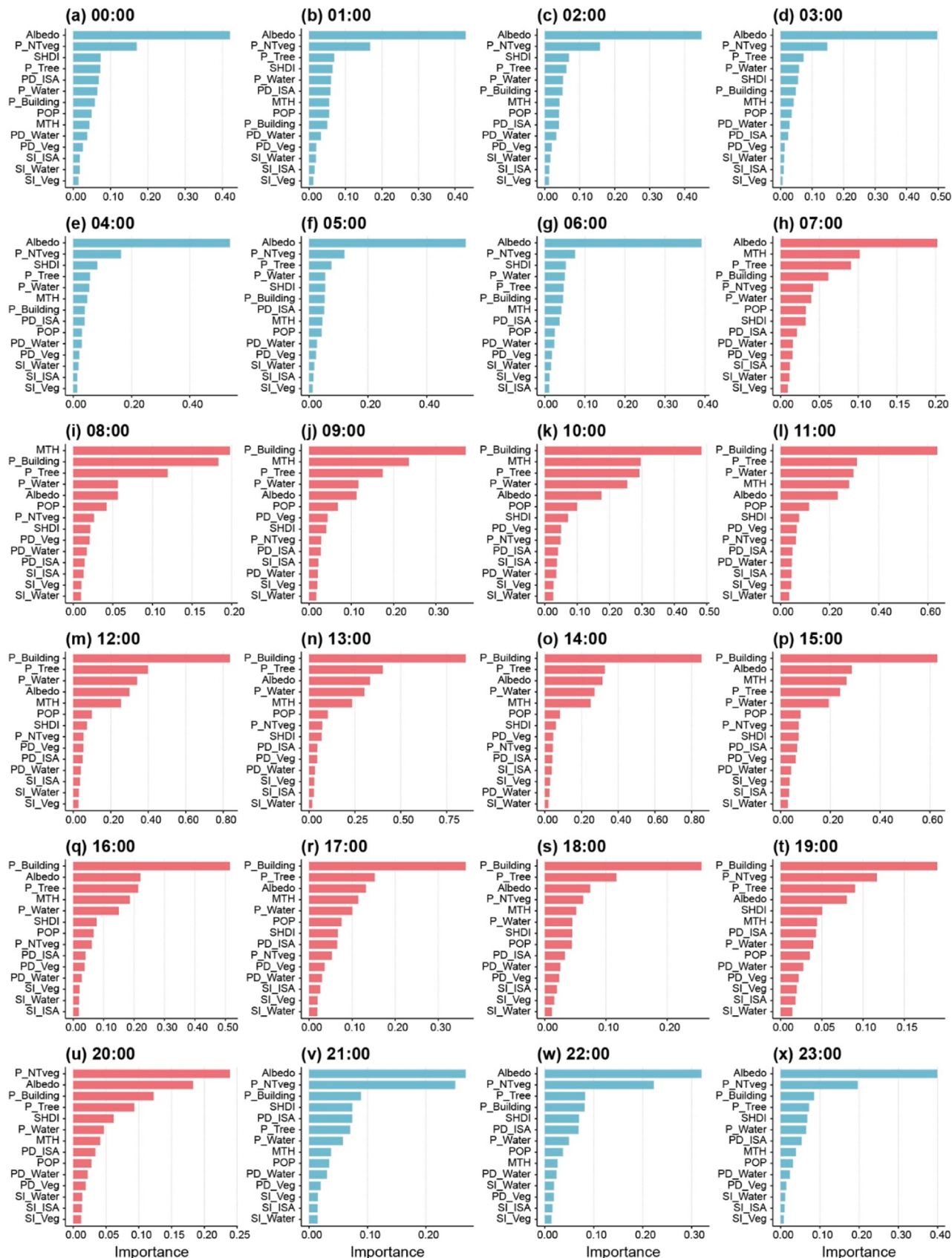


Fig. 6. Permutation-based importance of urban features to 24-hour LSTs. (a)–(x) represent the relative importance of urban features to LST on 00:00–23:00 EST time (local time). Importance value of a variable is the RMSE loss on model prediction when this variable is randomly shuffled. The blue bars represent importance of urban features to LST in the nighttime; the red bars represent importance of urban features to LST in the daytime.

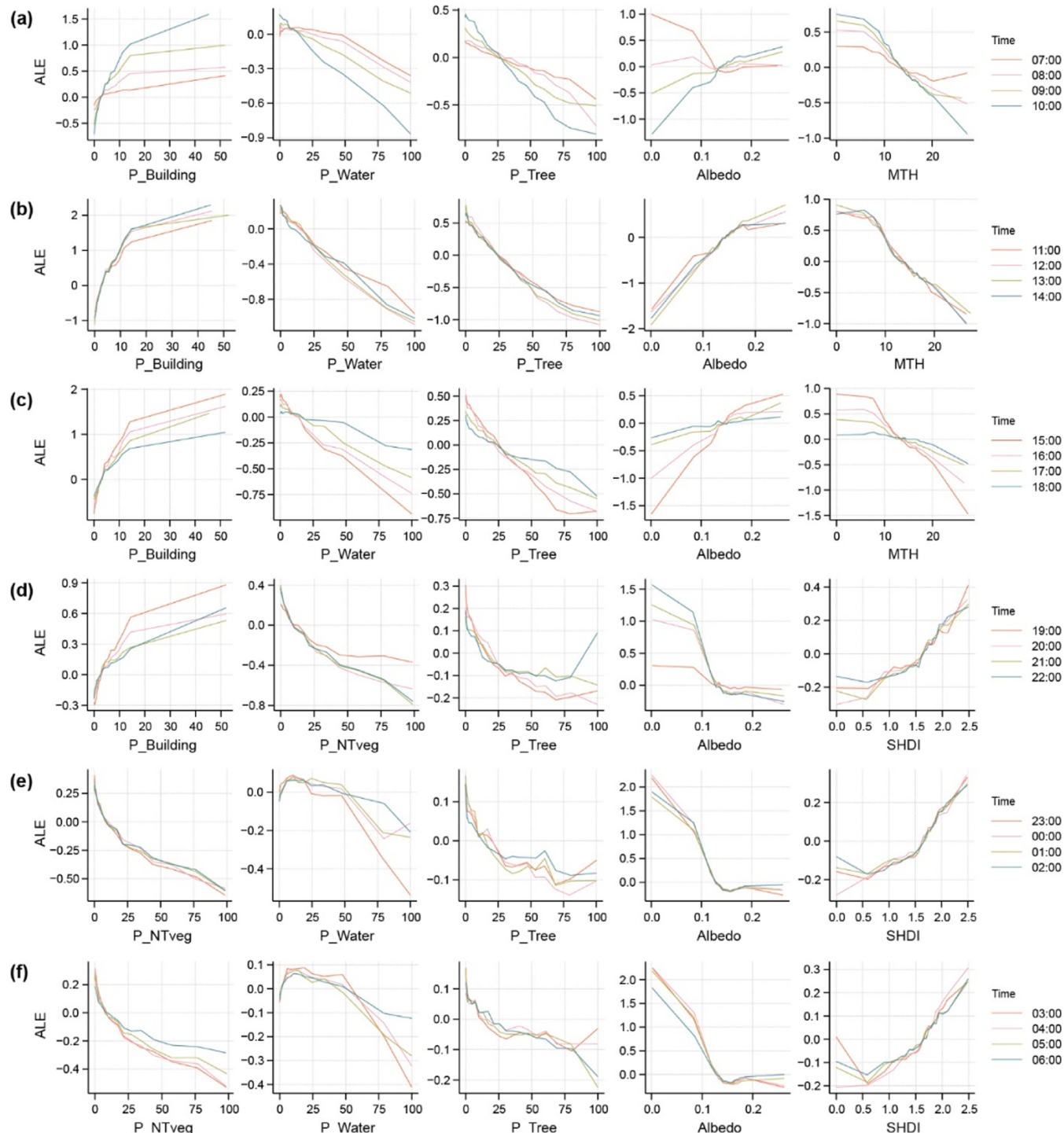


Fig. 7. Correlation curves between urban features and LST: insights from accumulated local effects (ALE) plots. Each of (a)–(f) listed the 5 most influencing factors in four hours based on their importance value (Fig. 6). The time grouping of (a)–(f) was based on the similarity of urban feature importance ranking and continuity of time. Basically, (a)–(c) are the daytime ALE plots, and (d)–(f) are the nighttime ALE plots.

Always Negative: Variables like P_NTveg, P_Tree, and P_Water demonstrated a continuous cooling effect on LST. At noon, water bodies and trees can reduce LST by 1–2 °C. (3) Day-night pattern: Some urban features exhibited effects that differ between day and night. For example, Albedo increased LST during the day but decreased it at night, while MTH lowered LST during the day and slightly increased it at night. Both Albedo and MTH showed maximum effects exceeding 2.5 °C. (4) Certain features, primarily landscape patterns such as PD and SI of different land covers, did not show clear trends or obvious impact on

LST.

5. Discussion

5.1. Model performance

In this study, we employed a Gradient Boosting Machine (GBM) model to decode the intricate non-linear associations between urban features and hourly diurnal LST variations. Leveraging cloud-based

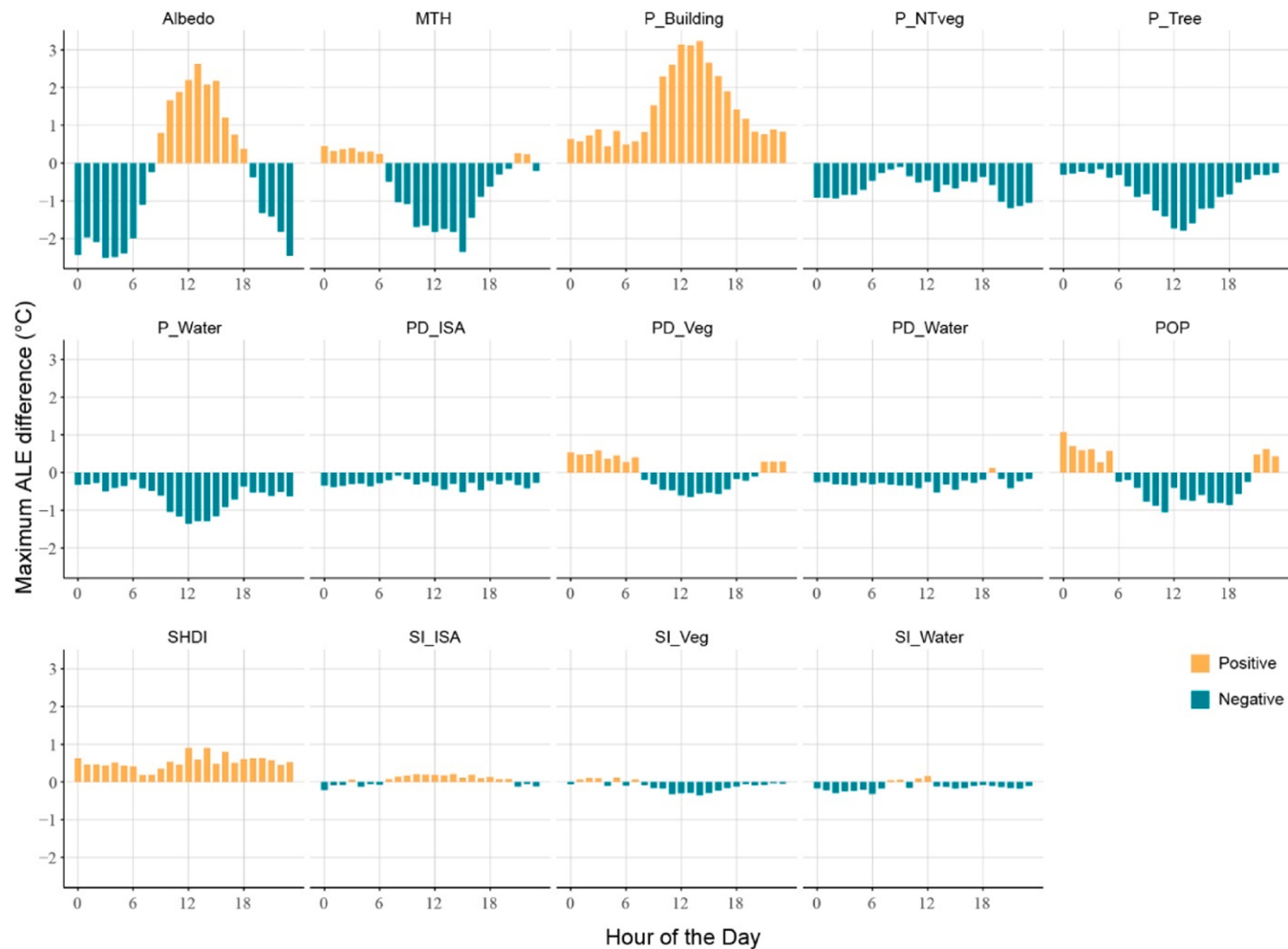


Fig. 8. Maximum ALE differences hourly trend for urban features. Positive impacts are highlighted in yellow, while negative impacts are highlighted in green.

computing, we aggregated thousands of satellite images and synthesized information from millions of building vectors to enhance the robustness of our analysis. Given the extensive longitudinal and latitudinal expanse of our study area, which introduces variability in climatic conditions and significantly influence analysis results, we incorporated three geo-climatic condition factors as control variables to account for these variations.

Prior research has established a strong correlation between specific urban features and LST, particularly noted at approximately 10:00 AM, the typical acquisition time for Landsat imagery (Lin et al., 2023; Logan et al., 2020; Smith et al., 2023; Wang et al., 2022). Extending upon these findings, our aim was to elucidate this relationship across the entire 24-hour cycle. Our results confirm the efficiency of GBM model in capturing the persistent link between urban features and LST at all hours, despite observable fluctuations in correlation strength throughout the day. This association persisted even after the exclusion of geoclimatic variables, underscoring the inherent connection between urban features and thermal profiles. To dissect the specific correlation patterns between various urban features and LST, we utilized permutation-based importance metrics (Fig. 6) and Accumulated Local Effect (ALE) plots (Fig. 7).

5.2. Impact of urban features on 24-hour LSTs

5.2.1. Landscape compositions

Our results showed urban areas exhibited rapid temperature fluctuations at daytime. In contrast, water bodies and vegetated areas

maintained more stable temperature profiles (Fig. 5). Analysis revealed a positive correlation between building coverage (P_Building) and LST, whereas urban blue-green spaces (P_Water, P_Tree) exhibit an inverse relationship throughout the diurnal cycle—although the influence lowered at night (Figs. 7 and 8). Similar findings have been observed in studies conducted during one or two hours of the day in various locations, including Portland (Logan et al., 2020), Shenzhen (Peng et al., 2018) and Tehran (Bokaie, Zarkesh, Arasteh & Hosseini, 2016). The observed variance in diurnal temperature dynamics across different landscape types is fundamentally linked to their unique thermal properties (Oke et al., 2017). Urban materials characterized by lower heat capacities and higher thermal conductivities precipitate rapid temperature changes (Mohajerani, Bakaric & Jeffrey-Bailey, 2017). Conversely, the substantial thermal buffering capacity of water bodies moderates local temperature fluctuations, allowing them to absorb and dissipate heat with minimal thermal disruption (Tan, Sun, Huang, Yuan & Hou, 2021). This thermal regulation is further augmented by the process of evapotranspiration, a dual mechanism involving evaporation from water bodies and transpiration from vegetation. Evaporation cools the air by absorbing heat, thereby lowering temperatures throughout the day. Concurrently, vegetation contributes to daytime cooling by transpiring water vapor via leaf stomata, reinforcing the role of natural landscapes in moderating LST (Gao, Santamouris & Feng, 2020). At nighttime, evapotranspiration rates are significantly lowered due to the absence of sunlight and closure of stomata of vegetations, leading the influence of urban blue-green spaces to LST lowered.

Furthermore, ALE plots of P_Building reveal significant non-linear

correlations with LST, characterized by upward concave shapes during the daytime. The behavior observed between 10:00 and 11:00 aligns with findings from previous non-linear analyses in Beijing (Han et al., 2023), Wuhan (Li et al., 2021), Shanghai (Sun, Liu, Wang, Wang & Che, 2020) and Barcelona (Lemus-Canovas et al., 2020). This observation suggests that the integrity of natural landscapes is inversely associated with the propensity for increased temperatures, indicating that even a modest degree of construction within green spaces can result in marked temperature elevations in altered regions. It is noteworthy that during peak temperature hours, the marginal effects of P_Building escalated to a maximum of 3 °C, surpassing all other times. This finding aligns with our sample analysis in Cleveland, which demonstrated that densely constructed areas are particularly susceptible to extreme temperature events.

5.2.2. Landscape patterns

Landscape patterns exerted a relatively minor influence on LST, aligning with the findings of several case studies across various cities utilizing Landsat LST data (Lu et al., 2023; Peng et al., 2018; Wang et al., 2022) and ECOSTRESS LST measurements (Lin et al., 2023), as well as investigations spanning a broader array of sites (Wu et al., 2022). The nuanced, indirect or paradoxical role of landscape configurations on LST may account for these observations (Zhou et al., 2011). For instance, large, contiguous vegetative areas typically register lower temperatures than their fragmented, diminutive counterparts, attributable to superior evapotranspiration efficiency (Cao, Onishi, Chen & Imura, 2010). Conversely, the dispersal of trees paradoxically enhances shading, thereby reducing LST compared to conditions where vegetation is clustered (Li, Yang & Lam, 2012). Notably, the Shannon diversity index (SHDI) emerges as a significant correlate with nocturnal LST within our dataset. This effect is primarily due to the minimal LST disparity among land covers during the night. Conversely, during daylight, when solar radiation significantly heats urban surfaces, the inherent thermal properties of land cover materials surpass the moderating effects of landscape diversity. This dynamic underscores the pivotal role of material composition in dictating daytime urban heat, challenging the efficacy of landscape diversity in tempering peak daytime temperatures. Despite localized studies emphasizing the significant impact of landscape configurations under specific climatic conditions, such as in Fuzhou (Lin et al., 2024) and Beijing (Zhang et al., 2023), our broader analysis reaffirms their limited overall influence.

5.2.3. Socio-economic factors

Socio-economic factors, notably population density (POP), are often interpreted as indicators of anthropogenic heat contributions. While Song et al. (2020) identified a correlation between POP and LST using a simple linear analysis, broader multifactorial studies have not substantiated POP as a primary driver of LST spatial variability such as studies at Chennai, Dhaka, Kolkata (Lu et al., 2023) and Xi'an (Chen et al., 2023). These investigations, although relying on Landsat imagery captured at a single daytime hour, align with our findings across a comprehensive 24-hour cycle. Similar to observations regarding landscape patterns, the relatively modest correlation between population density and LST may stem from the indirect mechanisms through which population influences material surface heat.

5.2.4. Surface albedo

Materials characterized by low surface albedo typically exhibit reduced solar reflectance, thereby absorbing more heat and potentially reaching higher temperatures (Trlica, Hutyra, Schaaf, Erb & Wang, 2017). Interestingly, certain low-albedo materials, such as water, with albedo values ranging from 0.06 to 0.1, counter this trend by employing evaporation to effectively lower surface temperatures, thus demonstrating a deviation from the expected heat absorption behavior (Tan et al., 2021). These contrasting mechanisms—heat absorption versus evaporative cooling—dictate the impact of albedo on surface

temperature in a dynamic manner. Our findings indicate a dominant influence of evaporative cooling during daytime, resulting in a positive correlation between surface albedo and LST. This observation corroborates similar research conducted in Kolkata and Dhaka, utilizing Landsat-derived LST data (10:00 A.M.) (Lu et al., 2023). Conversely, nighttime conditions, characterized by a reduction in evaporative processes, reveal that low-albedo surfaces, including water bodies, buildings, and roadways, begin to release accumulated heat. This shift manifests as a negative correlation between albedo and LST, underscoring singular effect of albedo on temperature modulation in the absence of evaporative cooling. The high temporal resolution of our study allowed for the detailed observation of the transitional effects attributed to evaporative cooling as influenced by solar radiation intensity. Specifically, dawn and dusk periods—illustrated in Figures 7(a) and 7(c), respectively—highlight a progressive shift in the albedo-LST relationship. During periods of intense sunlight, a strong positive correlation was observed, which diminishes as sunlight wanes, eventually inverting to a negative correlation with the onset of night.

5.2.5. Tree canopy height

The influence of mean tree height (MTH) on LST exhibited a pronounced diurnal variation. Our analysis indicates that the impact of MTH on LST was negligible during nocturnal hours but became rapidly significant with sunrise, maintaining its status as a key modulator of LST throughout the day until diminishing at dusk. This trend suggests a close alignment between the effect of MTH and solar irradiance, mirroring patterns observed with P_Building. Importantly, MTH demonstrated a negative correlation with daytime LST, with its influence notably stronger in the morning compared to the afternoon (Fig. 6). This pattern suggests that tree shading could be a primary mechanism through which MTH modulates LST, as proposed by Wu et al. (2022). The underlying mechanism appears to be related to the differential warming rates between shaded and unshaded urban areas. In the morning, as sunlight begins to warm the cityscape, areas under tree cover remain cooler. However, as the day progresses and solar elevation changes modify shadow lengths and directions, these cooler, shaded areas start to warm, reducing the temperature differential between shaded and sun-exposed surfaces.

5.3. Urban planning implications

Our study outlines innovative approaches for urban heat island UHI mitigation, with a focus on comprehensive 24-hour and highest sunlight intensity time temperature regulation. We reveal that urban areas, particularly those lacking sufficient vegetation and water bodies, experience disproportionately higher temperatures during peak heat hours compared to rural areas, highlighting the crucial role of integrating green and blue spaces within densely constructed regions to mitigate heat-related risks. Such integration not only addresses extreme heat events but also contributes to the overall regulation of diurnal LST fluctuations. Notably, our analysis, informed by ALE plots, reveals that even minimal urban development within natural landscapes can precipitate rapid LST escalations, emphasizing the necessity of preserving substantial, undisturbed natural environments such as large parks, forests and lakes etc. Furthermore, the application of high-albedo materials emerges as a vital strategy for reflecting solar radiation and minimizing heat absorption, significantly reducing LST across the diurnal cycle. In addressing the design and orientation of urban structures, our study suggests the strategic deployment of tall buildings and trees to maximize shadow coverage on streets, enhancing road temperature control and urban ventilation. However, caution is advised with tall buildings, which may retain heat during the day and release it at night, potentially exacerbating nocturnal heat issues (Wang et al., 2023). Where economic or social constraints limit the implementation of these primary measures, adjustments in landscape patterns and population density offer alternative pathways for urban temperature management. This

comprehensive approach underlines the need for holistic urban planning strategies that address both immediate heat challenges and the overarching goal of fostering resilient, sustainable urban environments in response to climate change.

5.4. Limitations

This study extends the time resolution of previous research from isolated hours of a day to a comprehensive hour-by-hour analysis and expands the scope from single or a few cities to dozens of cities, enhancing its generalizability. However, it has several limitations. The exclusive reliance on GOES-16 satellite imagery, while providing exceptional temporal resolution, confines the geographical applicability of our findings to North America. Additionally, although we employed the VIF test and ALE plots to minimize multicollinearity, it does not eliminate it entirely; the complex interactions between urban features still influenced model performance. Due to computational speed limitations, many machine learning-based studies on urban feature-LST correlations remain restricted to single or a few cities. Future research should utilize cloud computing to broaden the geographical scope of analysis and incorporate a wider range of satellite datasets to cover diverse urban environments globally. Such an expansion would not only deepen our understanding of urban heat islands on a global scale but also support the development of more targeted and effective urban planning strategies across various climatic and geographic contexts.

6. Conclusion

To assist urban planners tackling climate change and UHI induced city over warming, we see to determine the intricate relationship between urban features and LST during 24-hour cycle. Leveraging GBM model, we demonstrated the paramount influence of certain urban features on LST, with their effects markedly modulating in response to the sunlight variation in each hour. Our findings underscore the pivotal role of urban features with direct interactions with sunlight — such as surface albedo, building coverage, urban blue-green space and 3D structure (casting shadows) — in shaping the thermal landscape of urban areas, each contributing to the thermal variance observed through 24-hour cycles. We identified two distinct patterns in how urban

features affect LST: a nocturnal pattern, where the relationship between urban features and LST remains consistent across night hours, and a diurnal pattern, where this correlation fluctuates with sunlight intensity. Particularly during peak temperature hours, building coverage significantly increases LST, suggesting urban centers are more vulnerable to heat extremes. This highlights the dual nature of urban development: while it is vital for supporting growing urban populations, it unmistakably intensifies the UHI effect, especially during periods of intense sunlight. The methodologies employed and results obtained from this study contribute significantly to the burgeoning discourse on sustainable urban planning and climate resilience. By identifying the diurnal variations in the impact of urban features on LST, our research offers a critical lens through which urban planners and policymakers can strategize interventions aimed at mitigating UHIs.

CRediT authorship contribution statement

Qi Wang: Writing – original draft, Visualization, Supervision, Methodology, Formal analysis. **Haitao Wang:** Writing – review & editing, Validation, Investigation, Data curation. **Lanhong Ren:** Writing – review & editing, Validation, Funding acquisition. **Jianli Chen:** Resources, Investigation. **Xiaona Wang:** Writing – review & editing.

Declaration of competing interest

The authors declare that they have no known competing financial interests or personal relationships that could have appeared to influence the work reported in this paper.

Data availability

Data will be made available on request.

Acknowledgement

This work was supported by National Natural Science Foundation of China [grant number 52208019].

Appendices

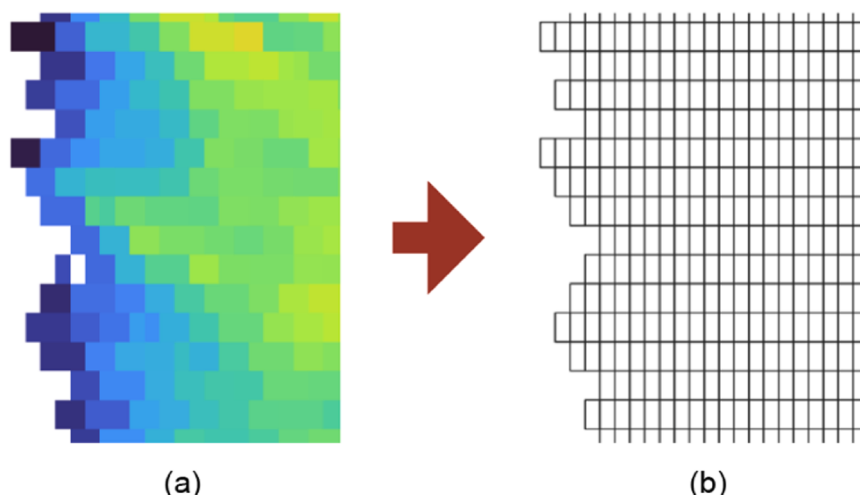


Fig. A1. The process of transforming LST raster data into polygonized analytical units.

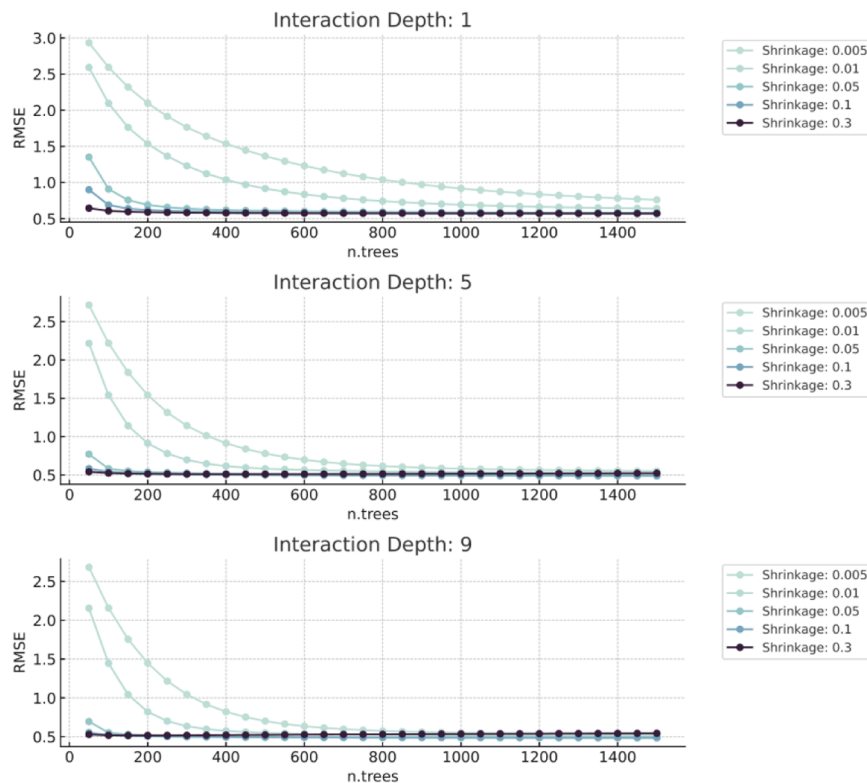


Fig A2. Hyperparameters tuning grid using repeated cross-validation. Three hyperparameters were fine tuned in our model, namely depth of the tree (interaction depth in ‘caret’ package of R), number of trees (n.trees in ‘caret’), and learning rate (shrinkage in ‘caret’). Hyperparameters combination with the lowest RMSE values were deemed as the best model.

References

- Adeyeri, O. E., Folorunsho, A. H., Ayegbusi, K. I., Bobde, V., Adeliyi, T. E., Ndehedehe, C. E., & Akinsanola, A. A. (2024). Land surface dynamics and meteorological forcings modulate land surface temperature characteristics. *Sustainable Cities and Society*, 101, Article 105072. <https://doi.org/10.1016/j.scs.2023.105072>
- Alexander, C. (2021). Influence of the proportion, height and proximity of vegetation and buildings on urban land surface temperature. *International Journal of Applied Earth Observation and Geoinformation*, 95, Article 102265. <https://doi.org/10.1016/j.jag.2020.102265>
- Beck, H. E., Zimmermann, N. E., McVicar, T. R., Vergopolan, N., Berg, A., & Wood, E. F. (2018). Present and future Köppen-Geiger climate classification maps at 1-km resolution. *Scientific Data*, 5(1), 1–12.
- Bera, D., Chatterjee, N. D., Ghosh, S., Dinda, S., & Bera, S. (2022). Recent trends of land surface temperature in relation to the influencing factors using Google Earth Engine platform and time series products in megacities of India. *Journal of Cleaner Production*, 379, Article 134735. <https://doi.org/10.1016/j.jclepro.2022.134735>
- Bokaie, M., Zarkesh, M. K., Arasteh, P. D., & Hosseini, A. (2016). Assessment of Urban Heat Island based on the relationship between land surface temperature and Land Use/Land Cover in Tehran. *Sustainable Cities and Society*, 23, 94–104. <https://doi.org/10.1016/j.scs.2016.03.009>
- Botje, D., Dewan, A., & Chakraborty, T. C. (2022). Comparing coarse-resolution land surface temperature products over Western Australia. *Remote Sensing*, 14(10), Article 10. <https://doi.org/10.3390/rs14102296>
- Burke, M., Hsiang, S. M., & Miguel, E. (2015). Global non-linear effect of temperature on economic production. *Nature*, 527(7577), 235–239.
- Cai, X., Yang, J., Zhang, Y., Xiao, X., & Xia, J. (Cecilia) (2023). Cooling island effect in urban parks from the perspective of internal park landscape. *Humanities and Social Sciences Communications*, 10(1). <https://doi.org/10.1057/s41599-023-02209-5>. Article 1.
- Cao, X., Onishi, A., Chen, J., & Imura, H. (2010). Quantifying the cool island intensity of urban parks using ASTER and IKONOS data. *Landscape and Urban Planning*, 96(4), 224–231. <https://doi.org/10.1016/j.landurbplan.2010.03.008>
- Chang, Y., Xiao, J., Li, X., Froliking, S., Zhou, D., Schneider, A., Weng, Q., Yu, P., Wang, X., Li, X., Liu, S., & Wu, Y. (2021). Exploring diurnal cycles of surface urban heat island intensity in Boston with land surface temperature data derived from GOES-R geostationary satellites. *Science of The Total Environment*, 763, Article 144224. <https://doi.org/10.1016/j.scitotenv.2020.144224>
- Chen, D., Zhang, F., Zhang, M., Meng, Q., Jim, C. Y., Shi, J., Tan, M. L., & Ma, X. (2022). Landscape and vegetation traits of urban green space can predict local surface temperature. *Science of The Total Environment*, 825, Article 154006. <https://doi.org/10.1016/j.scitotenv.2022.154006>
- Chen, X., Wang, Z., Bao, Y., Luo, Q., & Wei, W. (2022). Combined impacts of buildings and urban remnant mountains on thermal environment in multi-mountainous city. *Sustainable Cities and Society*, 87, Article 104247. <https://doi.org/10.1016/j.scs.2022.104247>
- Chen, Y., Yang, J., Yu, W., Ren, J., Xiao, X., & Xia, J. C. (2023). Relationship between urban spatial form and seasonal land surface temperature under different grid scales. *Sustainable Cities and Society*, 89, Article 104374. <https://doi.org/10.1016/j.scs.2022.104374>
- Dewan, A., Kiselev, G., Botje, D., Mahmud, G. I., Bhuiyan, Md. H., & Hassan, Q. K. (2021). Surface urban heat island intensity in five major cities of Bangladesh: Patterns, drivers and trends. *Sustainable Cities and Society*, 71, Article 102926. <https://doi.org/10.1016/j.scs.2021.102926>
- Dewitz, J. (2023). National Land Cover Database (NLCD) 2021 products: US geological survey data release. <https://doi.org/10.5066/P9JZTA03>.
- Estoque, R. C., Murayama, Y., & Myint, S. W. (2017). Effects of landscape composition and pattern on land surface temperature: An urban heat island study in the megacities of Southeast Asia. *Science of The Total Environment*, 577, 349–359. <https://doi.org/10.1016/j.scitotenv.2016.10.195>
- Fisher, A., Rudin, C., & Dominici, F. (2019). All models are wrong, but many are useful: Learning a variable’s importance by studying an entire class of prediction models simultaneously. *Journal of Machine Learning Research*, 20(177), 1–81.
- Friedman, J. H. (2001). Greedy function approximation: A gradient boosting machine. *The Annals of Statistics*, 29(5), 1189–1232.
- Gao, K., Santamouris, M., & Feng, J. (2020). On the cooling potential of irrigation to mitigate urban heat island. *Science of the Total Environment*, 740, Article 139754. <https://doi.org/10.1016/j.scitotenv.2020.139754>
- Gasparrini, A., Guo, Y., Sera, F., Vicedo-Cabrera, A. M., Huber, V., Tong, S., Coelho, M., de, S. Z. S., Saldiva, P. H. N., Lavigne, E., & Correa, P. M. (2017). Projections of temperature-related excess mortality under climate change scenarios. *The Lancet Planetary Health*, 1(9), e360–e367.
- Guha, S., Govil, H., Dey, A., & Gill, N. (2018). Analytical study of land surface temperature with NDVI and NDBI using Landsat 8 OLI and TIRS data in Florence and Naples city, Italy. *European Journal of Remote Sensing*, 51(1), 667–678. <https://doi.org/10.1080/22797254.2018.1474494>
- Han, D., An, H., Cai, H., Wang, F., Xu, X., Qiao, Z., Jia, K., Sun, Z., & An, Y. (2023). How do 2D/3D urban landscapes impact diurnal land surface temperature: Insights from block scale and machine learning algorithms. *Sustainable Cities and Society*, 99, Article 104933. <https://doi.org/10.1016/j.scs.2023.104933>
- Herfort, B., Lautenbach, S., Porto De Albuquerque, J., Anderson, J., & Zipf, A. (2023). A spatio-temporal analysis investigating completeness and inequalities of global

- urban building data in OpenStreetMap. *Nature Communications*, 14(1), 3985. <https://doi.org/10.1038/s41467-023-39698-6>
- Hesselbarth, M. H., Sciaim, M., With, K. A., Wiegand, K., & Nowosad, J. (2019). landscapemetrics: An open-source R tool to calculate landscape metrics. *Ecography*, 42(10), 1648–1657.
- Ho, H. C., Knudby, A., Sirovayk, P., Xu, Y., Hodul, M., & Henderson, S. B. (2014). Mapping maximum urban air temperature on hot summer days. *Remote Sensing of Environment*, 154, 38–45. <https://doi.org/10.1016/j.rse.2014.08.012>
- Kashki, A., Karami, M., Zandi, R., & Roki, Z. (2021). Evaluation of the effect of geographical parameters on the formation of the land surface temperature by applying OLS and GWR, A case study Shiraz City, Iran. *Urban Climate*, 37, Article 100832. <https://doi.org/10.1016/j.ulclim.2021.100832>
- Lemus-Canovas, M., Martin-Vide, J., Moreno-Garcia, M. C., & Lopez-Bustins, J. A. (2020). Estimating Barcelona's metropolitan daytime hot and cold poles using Landsat-8 Land Surface Temperature. *Science of the Total Environment*, 699, Article 134307. <https://doi.org/10.1016/j.scitotenv.2019.134307>
- Li, D. H. W., Yang, L., & Lam, J. C. (2012). Impact of climate change on energy use in the built environment in different climate zones – A review. *Energy*, 42(1), 103–112. <https://doi.org/10.1016/j.energy.2012.03.044>
- Li, H., Li, Y., Wang, T., Wang, Z., Gao, M., & Shen, H. (2021). Quantifying 3D building form effects on urban land surface temperature and modeling seasonal correlation patterns. *Building and Environment*, 204, Article 108132. <https://doi.org/10.1016/j.buildenv.2021.108132>
- Li, Z., & Hu, D. (2022). Exploring the relationship between the 2D/3D architectural morphology and urban land surface temperature based on a boosted regression tree: A case study of Beijing, China. *Sustainable Cities and Society*, 78, Article 103392. <https://doi.org/10.1016/j.scs.2021.103392>
- Liang, S. (2001). Narrowband to broadband conversions of land surface albedo I: Algorithms. *Remote Sensing of Environment*, 76(2), 213–238.
- Lin, Z., Xu, H., Yao, X., Yang, C., & Yang, L. (2023). Exploring the relationship between thermal environmental factors and land surface temperature of a “furnace city” based on local climate zones. *Building and Environment*, 243, Article 110732. <https://doi.org/10.1016/j.buildenv.2023.110732>
- Lin, Z., Xu, H., Yao, X., Yang, C., & Ye, D. (2024). How does urban thermal environmental factors impact diurnal cycle of land surface temperature? A multi-dimensional and multi-granularity perspective. *Sustainable Cities and Society*, 101, Article 105190. <https://doi.org/10.1016/j.scs.2024.105190>
- Logan, T. M., Zaitchik, B., Guikema, S., & Nisbet, A. (2020). Night and day: The influence and relative importance of urban characteristics on remotely sensed land surface temperature. *Remote Sensing of Environment*, 247, Article 111861. <https://doi.org/10.1016/j.rse.2020.111861>
- Lu, L., Fu, P., Dewan, A., & Li, Q. (2023). Contrasting determinants of land surface temperature in three megacities: Implications to cool tropical metropolitan regions. *Sustainable Cities and Society*, 92, Article 104505. <https://doi.org/10.1016/j.scs.2023.104505>
- Massaro, E., Schifanella, R., Piccardo, M., Caporaso, L., Taubenböck, H., Cescatti, A., & Duveiller, G. (2023). Spatially-optimized urban greening for reduction of population exposure to land surface temperature extremes. *Nature Communications*, 14(1), 2903. <https://doi.org/10.1038/s41467-023-38596-1>
- Mohajerani, A., Bakaric, J., & Jeffrey-Bailey, T. (2017). The urban heat island effect, its causes, and mitigation, with reference to the thermal properties of asphalt concrete. *Journal of Environmental Management*, 197, 522–538. <https://doi.org/10.1016/j.jenvman.2017.03.095>
- Molnar, C. (2020). *Interpretable machine learning*. Lulu.com.
- NOAA. (2019). GOES-R series product definition and users' guide. <https://www.goes-r.gov/products/docs/PUG-L2+-vol5.pdf>.
- O'brien, R. M. (2007). A caution regarding rules of thumb for variance inflation factors. *Quality & Quantity*, 41(5), 673–690. <https://doi.org/10.1007/s11135-006-9018-6>
- Oke, T. R., Mills, G., Christen, A., & Voogt, J. A. (2017). *Urban Climates* (1st ed.). Cambridge University Press. <https://doi.org/10.1017/9781139016476>
- Pande, C. B., Egbaru, J. C., Costache, R., Sidek, L. M., Wang, Q., Alshehri, F., Din, N. M., Gautam, V. K., & Chandra Pal, S. (2024). Predictive modeling of land surface temperature (LST) based on Landsat-8 satellite data and machine learning models for sustainable development. *Journal of Cleaner Production*, 444, Article 141035. <https://doi.org/10.1016/j.jclepro.2024.141035>
- Peng, J., Jia, J., Liu, Y., Li, H., & Wu, J. (2018). Seasonal contrast of the dominant factors for spatial distribution of land surface temperature in urban areas. *Remote Sensing of Environment*, 215, 255–267. <https://doi.org/10.1016/j.rse.2018.06.010>
- Potapov, P., Li, X., Hernandez-Serna, A., Tyukavina, A., Hansen, M. C., Kommareddy, A., Pickens, A., Turubanova, S., Tang, H., Silva, C. E., Armstrong, J., Dubayah, R., Blair, J. B., & Hofton, M. (2021). Mapping global forest canopy height through integration of GEDI and Landsat data. *Remote Sensing of Environment*, 253, Article 112165. <https://doi.org/10.1016/j.rse.2020.112165>
- Ramakrishnan, S., Wang, X., Sanjayam, J., & Wilson, J. (2017). Thermal performance of buildings integrated with phase change materials to reduce heat stress risks during extreme heatwave events. *Applied Energy*, 194, 410–421.
- Refaeilzadeh, P., Tang, L., & Liu, H. (2009). Cross-validation. *Encyclopedia of Database Systems*, 5, 532–538.
- Ren, J., Yang, J., Wu, F., Sun, W., Xiao, X., & Xia, J.(Cecilia) (2023). Regional thermal environment changes: Integration of satellite data and land use/land cover. *iScience*, 26(2). <https://doi.org/10.1016/j.isci.2022.105820>
- Smith, I. A., Fabian, M. P., & Hutyra, L. R. (2023). Urban green space and albedo impacts on surface temperature across seven United States cities. *Science of The Total Environment*, 857, Article 159663. <https://doi.org/10.1016/j.scitotenv.2022.159663>
- Smith, R. (2010). *The heat budget of the earth's surface deduced from space*. New Haven, CT, USA: Yale University Center for Earth Observation.
- Song, J., Chen, W., Zhang, J., Zhang, Jianjun, Huang, K., Hou, B., & Prishchepov, A. V. (2020). Effects of building density on land surface temperature in China: Spatial patterns and determinants. *Landscape and Urban Planning*, 198, Article 103794. <https://doi.org/10.1016/j.landurbplan.2020.103794>
- Stevens, F. R., Gaughan, A. E., Linard, C., & Tatem, A. J. (2015). Disaggregating census data for population mapping using random forests with remotely-sensed and ancillary data. *PLoS One*, 10(2), Article e0107042. <https://doi.org/10.1371/journal.pone.0107042>
- Sun, F., Liu, M., Wang, Y., Wang, H., & Che, Y. (2020). The effects of 3D architectural patterns on the urban surface temperature at a neighborhood scale: Relative contributions and marginal effects. *Journal of Cleaner Production*, 258, Article 120706. <https://doi.org/10.1016/j.jclepro.2020.120706>
- Tan, X., Sun, X., Huang, C., Yuan, Y., & Hou, D. (2021). Comparison of cooling effect between green space and water body. *Sustainable Cities and Society*, 67, Article 102711. <https://doi.org/10.1016/j.scs.2021.102711>
- Tang, C., Liu, D., Tian, X., Zhao, F., & Dai, C. (2023). The variations of outgoing longwave radiation in East Asia and its influencing factors. *Atmosphere*, 14(3), Article 3. <https://doi.org/10.3390/atmos14030576>
- Trlica, A., Hutyra, L., Schaaf, C., Erb, A., & Wang, J. (2017). Albedo, land cover, and daytime surface temperature variation across an urbanized landscape. *Earth's Future*, 5(11), 1084–1101.
- Trost, J. E. (1986). Statistically nonrepresentative stratified sampling: A sampling technique for qualitative studies. *Qualitative Sociology*, 9(1), 54–57.
- Ullah, S., You, Q., Ullah, W., Sachindra, D. A., Ali, A., Bhatti, A. S., & Ali, G. (2023). Climate change will exacerbate population exposure to future heat waves in the China-Pakistan economic corridor. *Weather and Climate Extremes*, 40, Article 100570. <https://doi.org/10.1016/j.wace.2023.100570>
- Wang, Q., Wang, X., Meng, Y., Zhou, Y., & Wang, H. (2023). Exploring the impact of urban features on the spatial variation of land surface temperature within the diurnal cycle. *Sustainable Cities and Society*, 91, Article 104432. <https://doi.org/10.1016/j.scs.2023.104432>
- Wang, Q., Wang, X., Zhou, Y., Liu, D., & Wang, H. (2022). The dominant factors and influence of urban characteristics on land surface temperature using random forest algorithm. *Sustainable Cities and Society*, 79, Article 103722. <https://doi.org/10.1016/j.scs.2022.103722>
- Wei, G., He, B.-J., Liu, Y., & Li, R. (2024). How does rapid urban construction land expansion affect the spatial inequalities of ecosystem health in China? Evidence from the country, economic regions and urban agglomerations. *Environmental Impact Assessment Review*, 106, Article 107533. <https://doi.org/10.1016/j.eiar.2024.107533>
- Wu, W.-B., Yu, Z.-W., Ma, J., & Zhao, B. (2022). Quantifying the influence of 2D and 3D urban morphology on the thermal environment across climatic zones. *Landscape and Urban Planning*, 226, Article 104499. <https://doi.org/10.1016/j.landurbplan.2022.104499>
- Yan, H., Fan, S., Guo, C., Wu, F., Zhang, N., & Dong, L. (2014). Assessing the effects of landscape design parameters on intra-urban air temperature variability: The case of Beijing, China. *Building and Environment*, 76, 44–53. <https://doi.org/10.1016/j.buildenv.2014.03.007>
- Yao, X., Zhu, Z., Zhou, X., Shen, Y., Shen, X., & Xu, Z. (2022). Investigating the effects of urban morphological factors on seasonal land surface temperature in a “Furnace city” from a block perspective. *Sustainable Cities and Society*, 86, Article 104165. <https://doi.org/10.1016/j.scs.2022.104165>
- Yu, W., Yang, J., Sun, D., Xue, B., Sun, W., Ren, J., Yu, H., Xiao, X., Xia, J., & Li, X. (2024). Shared insights for heat health risk adaptation in metropolitan areas of developing countries. *iScience*, 27(5). <https://doi.org/10.1016/j.isci.2024.109728>
- Zeng, P., Sun, F., Liu, Y., Tian, T., Wu, J., Dong, Q., Peng, S., & Che, Y. (2022). The influence of the landscape pattern on the urban land surface temperature varies with the ratio of land components: Insights from 2D/3D building/vegetation metrics. *Sustainable Cities and Society*, 78, Article 103599. <https://doi.org/10.1016/j.scs.2021.103599>
- Zhang, M., Kafy, A.-A., Xiao, P., Han, S., Zou, S., Saha, M., Zhang, C., & Tan, S. (2023). Impact of urban expansion on land surface temperature and carbon emissions using machine learning algorithms in Wuhan, China. *Urban Climate*, 47, Article 101347. <https://doi.org/10.1016/j.ulclim.2022.101347>
- Zhang, M., Shukui, T., Zhang, C., & Chen, E. (2024). Machine learning in modelling the urban thermal field variance index and assessing the impacts of urban land expansion on seasonal thermal environment. *Sustainable Cities and Society*, Article 105345.
- Zhang, M., Tan, S., Liang, J., Zhang, C., & Chen, E. (2024). Predicting the impacts of urban development on urban thermal environment using machine learning algorithms in Nanjing, China. *Journal of Environmental Management*, 356, Article 120560. <https://doi.org/10.1016/j.jenvman.2024.120560>
- Zhang, M., Tan, S., Zhang, C., Han, S., Zou, S., & Chen, E. (2023). Assessing the impact of fractional vegetation cover on urban thermal environment: A case study of Hangzhou, China. *Sustainable Cities and Society*, 96, Article 104663. <https://doi.org/10.1016/j.scs.2023.104663>
- Zhang, R., Yang, J., Ma, X., Xiao, X., & Xia, J.(Cecilia) (2023). Optimal allocation of local climate zones based on heat vulnerability perspective. *Sustainable Cities and Society*, 99, Article 104981. <https://doi.org/10.1016/j.scs.2023.104981>
- Zhang, Z., Luan, W., Yang, J., Guo, A., Su, M., & Tian, C. (2023). The influences of 2D/3D urban morphology on land surface temperature at the block scale in Chinese

- megacities. *Urban Climate*, 49, Article 101553. <https://doi.org/10.1016/j.ulclim.2023.101553>
- Zhou, W., Huang, G., & Cadenasso, M. L. (2011). Does spatial configuration matter? Understanding the effects of land cover pattern on land surface temperature in urban landscapes. *Landscape and Urban Planning*, 102(1), 54–63. <https://doi.org/10.1016/j.landurbplan.2011.03.009>
- Zhou, W., Qian, Y., Li, X., Li, W.-J., Li, W., & Han, L. (2014). Relationships between land cover and the surface urban heat island: Seasonal variability and effects of spatial and thematic resolution of land cover data on predicting land surface temperatures. *Landscape Ecology*, 29(1), 153–167. <https://doi.org/10.1007/s10980-013-9950-5>